BIOPHYSICS

Rotation of endosomes demonstrates coordination of molecular motors during axonal transport

Luke Kaplan,[1] Athena Ierokomos,[1] Praveen Chowdary,[2] Zev Bryant,[3,4] Bianxiao Cui[2]*

Copyright © 2018 The Authors, some rights reserved; exclusive licensee American Association for the Advancement of Science. No claim to original U.S. Government Works. Distributed under a Creative Commons Attribution NonCommercial License 4.0 (CC BY-NC).

Long-distance axonal transport is critical to the maintenance and function of neurons. Robust transport is ensured by the coordinated activities of multiple molecular motors acting in a team. Conventional live-cell imaging techniques used in axonal transport studies detect this activity by visualizing the translational dynamics of a cargo. However, translational measurements are insensitive to torques induced by motor activities. By using gold nanorods and multichannel polarization microscopy, we simultaneously measure the rotational and translational dynamics for thousands of axonally transported endosomes. We find that the rotational dynamics of an endosome provide complementary information regarding molecular motor activities to the conventionally tracked translational dynamics. Rotational dynamics correlate with translational dynamics, particularly in cases of increased rotation after switches between kinesin- and dynein-mediated transport. Furthermore, unambiguous measurement of nanorod angle shows that endosome-contained nanorods align with the orientation of microtubules, suggesting a direct mechanical linkage between the ligand-receptor complex and the microtubule motors.

INTRODUCTION

Microtubule-dependent motor transport is one of the primary mechanisms that sustains polarized distributions of organelles and proteins in eukaryotic cells. It is particularly important in large and spatially compartmentalized cells like neurons, where diffusion is not a practical transport mechanism in an axon that can be as long as a meter. Unsurprisingly, dysregulation of axonal transport has been implicated in a variety of neurodegenerative disorders including Parkinson's disease, Huntingtin's disease, and Charcot-Marie-Tooth disease (*1*–*3*). Bidirectional axonal transport is powered by the microtubule-dependent motors, dynein and kinesin, tethering the cargos to microtubules and carrying them toward the cell body and the axonal terminus, respectively. It has been hypothesized that coordination between multiple motors ensures the robustness of long-range organelle transport. Consistent with this hypothesis, cargo run lengths increase 10-fold in vitro when powered by two copies of a given motor instead of one (*4*).

Cellular cargos can associate with multiple copies of both types of motors, and their collective activity results in the complex features of cargo motility (*5*–*8*). These features include changes in velocity, transient pauses, and direction reversals. The frequency of these events varies between individual cargos and is affected by genetic manipulations of motors and their regulatory factors (*9*, *10*). This inherent heterogeneity across cargos necessitates study by single-cargo analysis. Quantitative analysis of the dynamic features of cargo translational motion has been used to model the underlying behavior of the molecular motors (*11*–*13*). However, it is difficult to make significant conclusions about a complex system like axonal transport solely based on measuring translational dynamics. To wit, translational motion is degenerate in the sense that transport by different populations of active motors can result in seemingly identical motility patterns (*11*). Further, translational motion provides no information regarding the spatial distribution of motors on a given cargo, which has been suggested as an important factor in long-range transport (*14*).

Many causes have been proposed for the observed translational motion in axonal transport. These include regulated or stochastic detachment/attachment of cargo-bound motors from the microtubule [regulated (*1*, *9*, *10*) and stochastic (*11*, *15*)], elastic coupling between similar motors (*16*–*19*), and competition between opposite polarity motors (*6*, *11*). Experimentally discriminating between these using only translational motion has proven difficult but may be possible with additional experimental information.

For instance, Fig. 1 illustrates a hypothetical transporting endosome with three dyneins and one kinesin. At time zero (Fig. 1, dashed box), two dyneins are engaged with the microtubule, whereas the third dynein and the kinesin are in unbound states. A moment later, the states of some of the motors change, resulting in one of six scenarios (Fig. 1, conditions 1 to 6). Conditions 1 to 3 illustrate scenarios where the endosome pauses. Pauses can result from complete [condition 1 (*1*)] or partial [condition 2 (*20*, *21*)] detachment of motors from the microtubule. In these cases, the endosome rotational lability increases, whereas its translational motion is limited (*22*). Alternatively, there is evidence for regulatory factors halting motor walking but keeping them bound to the microtubule (*9*, *10*). This would result in pauses that are highly rotationally confined (condition 3).

Besides pausing, the endosome can also reverse direction, which would necessarily involve kinesin binding. This may result in a tug-of-war between the motors (*6*, *11*), causing an initial rotation followed by very little rotation (condition 4). Alternatively, it may require a regulated switch where dynein detaches in favor of kinesin, leaving the endosome fairly rotationally labile [condition 5 (*8*)]. Finally, binding and unbinding of motors can change parameters, such as transport speed (*23*), but could also influence orientation (condition 6).

We accomplish simultaneous tracking of rotational and translational motion of gold nanorod–labeled endosomes using polarized dark-field microscopy. Previous work tracking rotational motion with differential interference contrast microscopy was limited in two important respects (*22*). First, it was restricted to two polarization angles and therefore fourfold angle degeneracy. Second, it was carried out in conventional cell culture, limiting data throughput and sample size for statistical analysis. Dark-field microscopy with multipolarization channels allows millisecond time scale tracking with full azimuthal angular resolution in the range (0, 2π). For added data throughput and

[1]Biophysics Program, Stanford University, Stanford, CA 94305, USA. [2]Department of Chemistry, Stanford University, Stanford, CA 94305, USA. [3]Department of Bioengineering, Stanford University, Stanford, CA 94305, USA. [4]Department of Structural Biology, Stanford University, Stanford, CA 94305, USA.
*Corresponding author. Email: bcui@stanford.edu

Downloaded from http://advances.sciencemag.org/ on May 27, 2021

experimental control, we adopted a microfluidic culture platform that enables us to measure the behavior of a large number of individual endosomes. The high throughput is critical to the studies of highly heterogeneous systems such as axonal transport. We find that rotational motions of endosomes correlate with changes in cargo-microtubule connectivity. Unexpectedly, we also find that gold nanorods inside the endosomes are highly biased to align with microtubules on which they move, suggesting a previously unobserved mechanical linkage between the receptor-ligand complex and the microtubule track.

RESULTS

Multichannel dark-field microscopy can measure endosome orientation

Gold nanorods interact strongly with incident light due to excitation of a plasmon resonance along their geometric axes. As a result, light scattered by gold nanorods is polarized along these same axes of the nanorod and thus encodes its orientation (*24*). To exploit this property, we built a dark-field microscope to image the nanorods (Fig. 2A, i). Briefly, unpolarized white light is focused by a high–numerical aperture (NA) condenser (NA, 1.4) through a light stop that selects highly oblique rays to illuminate the sample. An adjustable NA objective (NA, ~1) collects only the scattered light, which is spectrally filtered to select the wavelength corresponding to light scattered by the long axis of the nanorod (650 nm). It is then split into either two (0, π/2) or three (0, π/4, π/2) polarization component angles and projected onto different parts of a scientific complementary metal-oxide semiconductor (sCMOS) camera at the image plane, akin to multicolor fluorescence channels. For each component polarization channel, nanorods appear as diffraction-limited spots (Fig. 2A, ii and iii), the intensity of which is proportional to the square of the cosine of the angle between the nanorod axis and the axis of the component polarization. Measuring the light intensities at two polarization channels enables determination of the azimuthal angle (ϕ) of the nanorod within one quadrant of the unit circle, whereas adding a third channel breaks the fourfold degeneracy to allow for determination of the angle on the interval (0, π) (see Materials and Methods). In principle, determination of the polar angle (θ) is also possible in our system (*25*) but is much less robust to noise in the cellular environment. Thus, we focus on ϕ in this work, hereafter referred to as "angle."

To validate our system for angle determination, we allowed nanorods to adsorb to glass coverslips and manually rotated the microscope stage through at least two revolutions (Fig. 2B). As shown in Fig. 2B (i) (top), the measured intensities of two channels (triangles) closely match the predictions (solid lines). The calculated angles from nanorod intensities agree well with the set angle of the stage, with a root mean square error less than 0.1 rad for most measurements (fig. S1). Two-channel microscopy only resolves orientation angles on the interval of (0, π/2), leaving the absolute direction of rotation ambiguous at the bounds of the interval (Fig. 2B, i). For instance, a nanorod initially at an angle of 0 can rotate 0.5 rad clockwise, but it will be indistinguishable from a nanorod that rotates 0.5 radians counterclockwise. Addition of the π/4 channel in three-channel microscopy allows for unambiguous resolution the orientation over the range (0, π). To break the remaining twofold symmetry of the nanorod, we track the angle at a rate faster than that required for the nanorod to rotate π radians (fig. S2, rotation of detached endosome, and movie S1). This enables angle determination over the full range (0, 2π) (Fig. 2B, ii). We note that total scattered

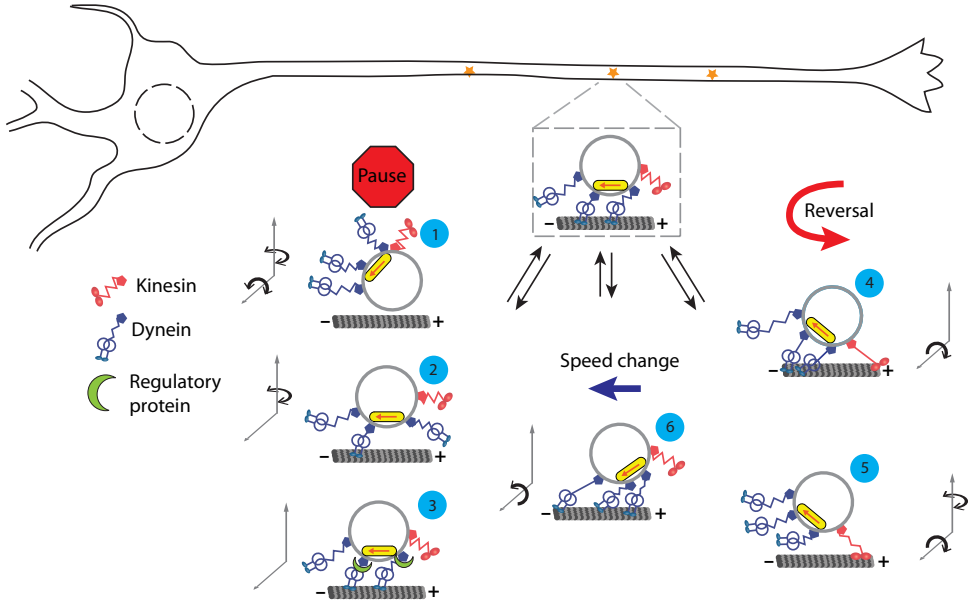

Fig. 1. Transport by teams of motors results in rotational dynamics. Schematic of a hypothetical endosome with three dyneins and one kinesin starts transporting in the configuration of the middle image (dashed box) and can transition to any of the states in conditions 1 to 6. In conditions 1 to 3, the translational motion is paused. In condition 1, the two previously bound dyneins unbind, and the cargo freely tumbles. However, the confinement of the axon restricts how far it will diffuse, making it difficult to detect significant diffusive translational motion. In condition 2, one of the motors detaches, leaving the endosome tethered to the microtubule but free to swivel. In condition 3, some regulatory factor [for example, Ndel1 (*9*)] halts processive motion of the motors, but they remain bound to the microtubule, restricting both translational and rotational motions. Conditions 4 and 5 illustrate two instances of direction reversal. In condition 4, the previously unbound kinesin binds and overpowers the dyneins in a tug-of-war. This manifests in an initial change in angle as the endosome rotates to relieve the torque of the kinesin binding, but the orientation is stable thereafter. In condition 5, the kinesin binds, whereas the dyneins unbind (*8*), and the endosome continues to rotate during subsequent motion. In condition 6, the previously unbound dynein becomes the leading motor exerting a torque on the endosome, causing an initial rotation as in condition 4. The new organization of the motor team causes a change in transport velocity.

Downloaded from http://advances.sciencemag.org/ on May 27, 2021

intensity remained constant throughout the rotation (black circles), consistent with total intensity being a function of polar angle and nanorod rotation restricted to the image plane. We also note that, although we can resolve orientations over the full azimuthal range, SE (blue error bars) depends on the nanorod angle and is slightly higher when one of the channels is near a minimum.

Two-channel imaging and three-channel imaging have important respective advantages. Three-channel imaging allows for symmetry breaking and determination of ϕ over its full range. Extra image splitting in three-channel imaging, however, results in lower signal intensity and thus a reduction of signal-to-noise ratio (SNR) in each channel compared to two-channel imaging (fig. S1). Consequently, precision is reduced in both angle determination and spatial localization. Furthermore, because imaging rate is limited by camera readout time, to maintain a fast frame rate, the imaging area is smaller for three-channel imaging as compared to two-channel imaging, reducing data collection throughput. Here, we use the larger imaging area and higher SNR of two-channel imaging for statistical analyses of rotational lability. For questions relating to the absolute angle of the nanorod, we use three-channel imaging.

Concurrent with determination of angular resolution, we determined the spatial precision of our microscope. Localization precision depends on the detected intensity of the nanorod in a given channel, which varies with angle. We first use the brightest available channel to determine the location with ~10-nm precision. Next, locations determined in different channels are mapped onto a single coordinate system using two-dimensional registration with a root mean square error of 30 nm in the *x* direction and 37 nm in the *y* direction (fig. S1 and section S1).

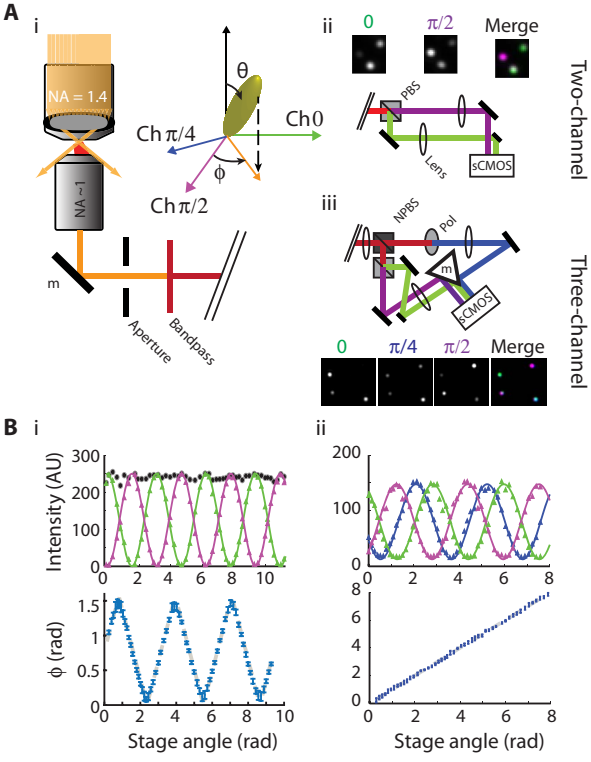

Fig. 2. Validation of multipolarization dark-field imaging for orientation determination. (**A**) Gold nanorods are excited identically in both two- and three-channel imaging, but their images are split in either two-component (ii) or three-component (iii) polarizations. Nanorods appear as diffraction-limited point spread functions. Ch, channel; PBS, polarizing beamsplitter; NPBS, nonpolarizing beamsplitter. (**B**) Calibration of azimuthal angle resolution for two-channel (i) and three-channel (ii) dark-field microscopy. Rotating the entire stage results in sinusoidal changes in intensity of individual nanorods (triangle data and line fit; i and ii, top). The calculated angle (i and ii, bottom, blue) matches well with the measured angle of the stage (gray). Error bars represent SD of the angle calculated for individual nanorods over a 75-frame movie. AU, arbitrary units.

Microfluidic cell culture provides a high-throughput platform for study of endosome transport

For axonal transport studies, we culture primary dorsal root ganglion (DRG) neurons in compartmentalized microfluidic devices (*26*). Briefly, dissociated DRG neurons are plated in the cell body compartment, close to the openings of microchannels. Their axons grow through the microchannels into the axon compartment, causing axons and consequently their microtubules to be unidirectionally aligned, facilitating distinction between kinesin- and dynein-mediated transport without tracing individual neurites to their cell bodies (Fig. 3A). The low channel height restricts axons in the *z* dimension and allows for use of higher NA objectives with shallower depth of field. When gold nanorods functionalized with wheat germ agglutinin (WGA) are added to either the cell body or the axon compartment, they bind to glycosylated cell surface proteins and undergo receptor-mediated endocytosis (Fig. 3B). Net retrograde transport of gold nanorods is achieved by incubation of WGA-nanorods in the axon compartment (Fig. 3C, i), and net anterograde transport is achieved with cell body compartment incubation (Fig. 3C, ii). The endosomes are then transported by molecular motors into the microchannels toward the opposite compartment. We exclusively image gold nanorods in microchannels where there are no free gold nanorods to interfere with imaging (Fig. 3B). The length of the microchannels assures that the observed transport is in the mid-axon, which is biochemically distinct from the termini or the initial segment (*27*–*29*). The microfluidic platform also facilitates high-throughput data acquisition, enabling us to collect 4374 endosome trajectories from the two-channel setup and 1703 trajectories from the three-channel setup.

Time-lapse movies in multichannel dark-field microscopy show clear rotational motions of transporting nanorods. Figure 3C shows kymographs of (i) a retrograde-directed endosome and (ii) an anterograde-directed endosome. The kymographs are generated by merging the 0 and π/2 polarization channels, colored in green and magenta, respectively. Both kymographs show typical transport patterns such as changes in speed, transient pauses, and occasional directional reversals. The nanorod intensity in a given polarization channel (for example, green) is fairly constant over hundreds of frames, indicating that the endosome is not rapidly rotating during transport. The intensities of the different polarization channels are used to calculate the orientation of the endosome (Fig. 3D, green). Notably, the nanorod maintains a relatively stable orientation during transport, albeit with small fluctuations, for prolonged periods of time interrupted by abrupt jumps in orientation. Several of these changes in orientation are clearly accompanied by changes in translational motion (orange arrow). There is not, however, a one-to-one correspondence between transitions in translational and rotational motions (black arrow). Instead, these two kinds of motion present overlapping but not redundant information about the underlying molecular motor activity.

Rotational dynamics are primarily due to molecular motor activity

To serve as a probe of endosome orientation, nanorods must not rotate with respect to the endosome, itself. To confirm this, we compared ro-

Downloaded from http://advances.sciencemag.org/ on May 27, 2021

tational lability of nanorods across environments that give different rotational constraint. When streptavidin-functionalized nanorods bind to a biotin-functionalized lipid bilayer, they exhibit extensive rotation, as shown in Fig. 4A (i). Similar fast rotational dynamics were observed when WGA-functionalized nanorods bound to the cell surface (Fig. 4A, ii). On the other hand, nanorods adsorbed to a glass surface show very little rotation as expected (Fig. 4A, iii). To determine where gold nanorods in endosomes fall between these two extremes, we obtained gold nanorod–containing endosomes from neurons. DRG neurons were incubated with WGA-nanorods together with a membrane-impermeable lipid dye, FM1-43. After washing and mechanical homogenization, the cell lysate was spread on a glass surface for subsequent rotational measurements. Nanorods inside endosomes can be distinguished from nonendocytosed nanorods by colocalization with the fluorescence signal from FM1-43 (Fig. 4B). Our measurements show that there is very little tumbling of nanorods inside endosomes, with rotational lability (Fig. 4A, iv), similar to that of nanorods adsorbed to glass. As a measure of rotational lability, we define a variable, σ, which is the SD of the nanorod angle in an 11-frame (66 ms) window. The size of this window is chosen to capture acute orientation changes with minimal blurring of signal (fig. S2). We pool the values of σ from all frames of many nanorods for each condition to calculate the cumulative distribution of rotational lability. As shown in Fig. 4C, the distribution of σ for nanorods in transporting endosomes (cyan curve) falls between nanorods on glass and nanorods on lipid bilayers. Nanorods rotate very little inside the endosome, as shown in the cumulative distribution of the purified endosomes (black curve). Therefore, the measured rotation during axonal transport is indicative of the endosome rotation instead of nanorods rotating inside endosomes.

Orientational changes can occur as either step changes from one stable orientation to another or changes in orientational fluctuation such as switching between a rotationally restricted state to a highly rotationally labile state (Fig. 4D and fig. S3). The first scenario can arise from switching the leading motor while the endosome remains bound to the microtubule during the switching (Fig. 1, condition 6). The second scenario can arise from complete or partial detachment to the microtubule track reducing the total connectivity restricting thermally driven tumbling (Fig. 1, conditions 1, 2, and 5). To assess how these two different rotational states contribute to the overall endosome rotation, we calculate the distribution of active rotation period lifetimes. These are defined as periods where the value of rotational lability, σ, for the endosome is continuously above 0.044, which is the 95th percentile of the σ distribution of purified endosomes on glass (dashed gray line in Fig. 4D). A histogram of lifetimes of active rotation periods in 1736 retrograde-directed endosome trajectories is well fit by a sum of two exponential distributions, with most rotations being the acute step variety ($\tau = 0.13$ s) and a minor fraction being longer periods of increased rotational lability ($\tau = 0.74$ s) (Fig. 4E). Consistent with this, we calculate the fraction of time that each endosome spends in a rotationally constrained state ($\sigma < 0.044$). A histogram of this data shows that endosomes spend the vast majority of their time in a rotationally restricted state (Fig. 4E, inset). When they do rotate, the rotations are sudden, consistent with stochastic changes in individual motor activity.

Rotation changes in correlation with translational motion

If the rotational motion of transporting endosomes arises from underlying microtubule motor activity, we would expect to see some correlation between rotational phenomena and translational motility. Accordingly, we separately quantified the rotational behavior during three distinct kinds of translational motion: changes in speed, pauses, and direction of transport. The first can arise because of stochastic changes in the team of motors without a switch in lead motor type. The second can arise either because of motor detachment or a stall in forward motion of the motors without detachment. The last is perhaps the most interesting because a change in transport direction can only result from a switch between kinesin- and dynein-mediated (or vice versa) transport.

Rotation correlates with changes in translational speed

We first confirmed that a clear correlation exists between translational and rotational motions after analyzing many endosomal trajectories. In individual trajectories, we frequently see that velocity changes temporally correlate with orientation changes (Fig. 5A). To statistically confirm this correlation, we computed the cross-correlation between the magnitude of changes in transport velocity (linear acceleration) and the magnitude of changes in orientation of nanorod-containing endosomes (angular velocity). For retrograde transport, the computed cross-

Downloaded from http://advances.sciencemag.org/ on May 27, 2021

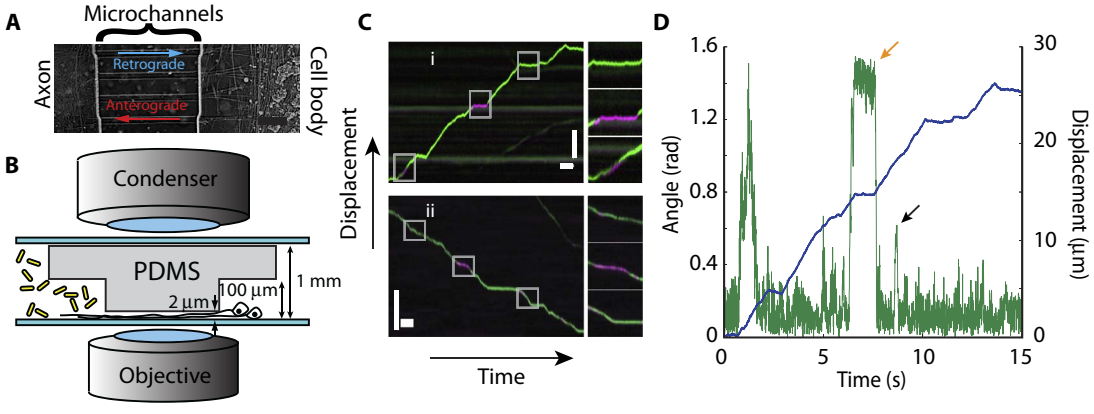

Fig. 3. Axonal transport of gold nanorods in microfluidic culture. (**A**) Neurons are plated close to the openings of microchannels into which they grow axons, which, therefore, have uniform directionality enabling unambiguous discrimination between dynein- and kinesin-mediated motion (scale bar, 100 µm). (**B**) WGA-nanorods are selectively added to the cell body or axon compartments where they are endocytosed and transported into the channels. Dark-field imaging is performed in the channels free from unbound and nonspecifically adsorbed nanorods. PDMS, polydimethylsiloxane. (**C**) Overlaying kymographs from 0 and π/2 polarization channels (green and magenta) show typical retrograde (i and movie S2) and anterograde (ii and movie S3) translational motion but also distinct rotational dynamics. Vertical scale bar, 5 µm; horizontal scale bar, 1 s. (**D**) Single-particle tracking of the endosome from (i) allows for precise angle (green) and position determination (blue).

correlation between the magnitudes of these vectors shows a significant peak around zero time. By comparison, time-scrambled control trajectories generated from the same set of data yield a flat cross-correlation showing no peak at time zero lag (Fig. 5B, top). When we calculate the same cross-correlation but include the sign of translational velocity changes (positive sign for retrograde direction and negative sign for anterograde), we find that there are opposite peaks on each side of zero lag (Fig. 5B, bottom). These data show that, for acceleration transitions, the angle change lags behind the velocity change. For deceleration transitions, the angle change precedes velocity changes.

The temporal correlation between orientation changes and velocity changes is also evident for endosomes transporting in the anterograde direction (Fig. 5C). Without considering the sign of the speed change, the cross-correlation plot shows a clear peak around zero, albeit to a lesser degree than retrograde transport. When the sign of the velocity change is considered, there are two peaks on each side of zero lag time. The peak directions are opposite of that for retrograde transport. As the anterograde transport direction is defined as negative, these data also show that the angle change lags behind the velocity change for acceleration transitions and the opposite for deceleration transitions (Fig. 5D). A reduced magnitude of the correlation in anterograde-directed cargo (relative to retrograde) is consistent with the observation that anterograde transport is often powered by as few as one to two kinesins, whereas retrograde transport requires several dyneins (*30*).

The local axonal environment could conceivably induce both translational and rotational motions of endosomes (by interactions with roadblocks, for instance). There is a correlation between motion perpendicular to the microtubule and angular velocity (fig. S4), but when we observe different endosomes passing through the same portion of an axon in short succession, their rotational motions are not identical as would be expected if local axonal environment was the dominant factor inducing these motions (fig. S5). Thus, it is unlikely that interactions with local axonal structures are the primary causes of the rotational motions we observe.

Rotation is constrained at pauses

The mechanisms for cargo pausing are the subject of much interest. Cargo pausing during axonal transport can be functionally important as in the case of mitochondria pausing due to calcium-regulated kinesin

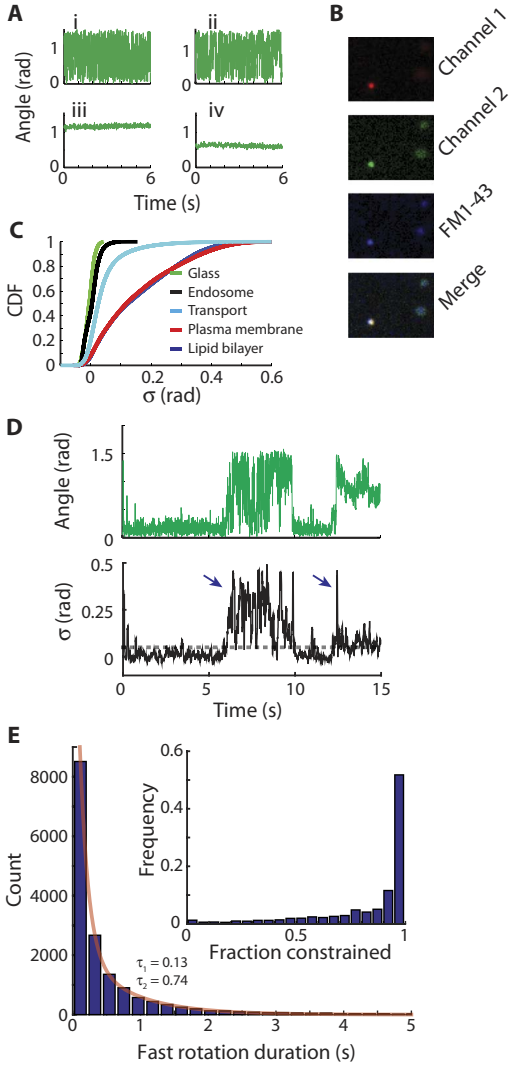

Fig. 4. Gold nanorods as effective in vivo rotational probes. (**A**) Nanorods attached to the plasma membrane (i) and supported bilayers (ii) show high rotational lability, whereas nanorods adsorbed to glass (iii) and WGA-nanorod-endosomes purified from neurons (iv) show much less rotational lability. (**B**) WGA-nanorod-endosomes are distinguished from free nanorods by colocalization with membrane staining FM1-43. (**C**) Cumulative distribution of σ from many nanorods ($n = 268$ for lipid bilayer, $n = 69$ for cell surface, $n = 27$ for glass surface, and $n = 13$ for endosome) confirms that there is minimal rotation of the nanorod with respect to the endosome. CDF, cumulative distribution function. (**D**) Example of an angle trace (top) converted into σ (bottom) with a long period of high rotational lability and a short one (arrows). Dashed gray line indicates σ = 0.044 above which is considered active rotation. (**E**) The duration of periods of increased rotational lability in processive retrograde trajectories shows that most are quite brief, and endosomes spend most of their time rotationally constrained (inset).

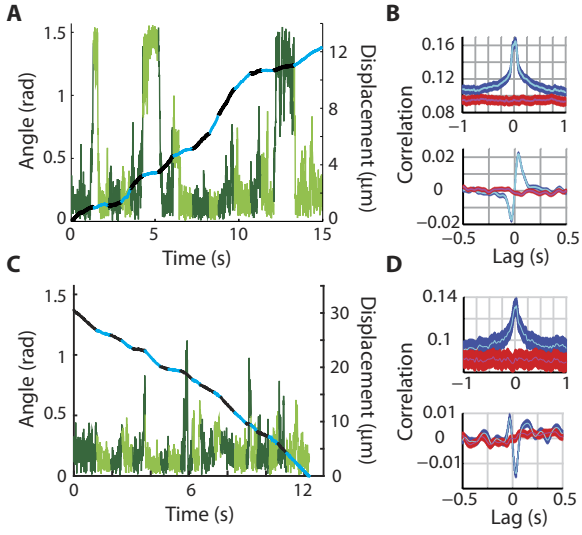

Fig. 5. Translational acceleration correlates with rotational dynamics. (**A**) Velocity changes in retrograde-directed endosomes often coincided with angle changes; discrete velocity segments colored alternating black and blue with corresponding orientations colored dark and light green (movie S4). (**B**) Mean cross-correlation between absolute (top) or directional (bottom) translational acceleration and angular velocity in retrograde endosomes shows pronounced peak (blue) relative to time-scrambled control (red) around zero lag (error bars ± SEM by bootstrapping). (**C** and **D**) Similar correlation between translational acceleration and rotational velocity is evident in anterograde-directed endosomes, although with slightly lower correlation.

Downloaded from http://advances.sciencemag.org/ on May 27, 2021

detachment from microtubules (*31*) or can result from dysfunction as in the case of CDK5-induced dynein tethering in models of amyotrophic lateral sclerosis (*10*). Rotational motion stands to differentiate between pauses resulting from increased tethering (Fig. 1, condition 3) and pauses resulting from detachment of motors (Fig. 1, conditions 1 and 2)—the former would show reduced rotational lability, whereas the latter would show increased rotation. We find that, during individual pauses within retrograde-directed [Fig. 6A (i) and movie S5] and anterograde-directed [Fig. 6A (ii) and movie S6] trajectories, endosomes do not show appreciably higher amounts of rotation than while actively transporting.

To statistically confirm this, we automatically detected 3654 pauses in 1087 individual otherwise processive retrograde transport trajectories (with two-channel microscopy) using transient motion analysis (*11*) and analyzed their rotational lability during the pausing periods. A box-whisker plot comparing the mean rotational lability during the pause against the pause duration shows that the rotational lability is independent of the length of the pause (Fig. 6B). In addition, the cumulative distribution of the rotational lability shows that there is very little difference between rotational lability at pauses and rotational lability during active transport [blue and black curves in Fig. 6C (top); P = 0.56 by Kolmogorov-Smirnov test; test statistic, 0.02]. There are fewer anterograde trajectories, and they pause less frequently (882 total trajectories and 1425 pauses, with 425 of those trajectories not pausing at all). Therefore, there are fewer detected long pauses, but it is clear that rotational lability is independent of the length of the pause in these endosomes as well (Fig. 6B, ii). The cumulative distribution of the rotational lability during pauses is similar to that during active anterograde transport [Fig. 6C, bottom (black and blue curves, respectively); P = 0.9 by Kolmogorov-Smirnov test; test statistic, 0.03]. Overall, our results show that axonal endosomes do not show either increased or decreased rotation during pauses, in contrast to previous findings in PC12 cells where transferrin-conjugated nanorods exhibited increased rotational dynamics during long pauses (*22*). This indicates that, in DRG axons, most pauses are not a result of endosome detachment.

Rotation increases at direction reversals

In sharp contrast to pauses, endosomes tend to increase overall rotation during transient reversals. The cumulative distribution shows increased rotational lability during segments of direction reversals, which is distinctive from that of active transport or pauses (red curve versus black and blue curves in Fig. 6C). This holds for endosomes traveling in net retrograde and net anterograde directions ($P < 0.0001$ for net retrograde and $P < 0.0001$ for net anterograde by Kolmogorov-Smirnov test). Although the rotational lability goes up in both cases, the magnitude of this effect is smaller for dynein-to-kinesin switching as compared with kinesin-to-dynein switching. Accordingly, the Kolmogorov-Smirnov test statistic is 0.06 for the former and 0.26 for the latter.

The increased rotation during a reversal is often evident even in individual traces (Fig. 7A and movie S7). The endosome in Fig. 7A maintained a stable orientation for most of its retrograde motion. However, direction reversals of this endosome were accompanied by a marked increase in the rotational lability of the endosome.

The observed increase in σ for reversals in Fig. 6C could potentially result if endosomes that undergo reversals are overall more rotationally labile. To test whether this is the case or the reversal periods themselves undergo increased rotation, we performed a paired analysis between the segments of trajectories where translational motion was directed versus reversals. Net retrograde trajectories that showed at least one period of pausing and reversal were automatically selected. The mean value of σ was calculated for each trajectory during its directed motion, pausing, and reversal. A value, Δσ, was obtained by taking the difference between the mean value of σ during directed motion and pauses ($\Delta\sigma_{pause}$) or between directed motion and reversals ($\Delta\sigma_{reversal}$). Pairing these values controls for possible differences in overall rotational lability between cargos. The distribution of this variable is shown in Fig. 7B. Notably, $\Delta\sigma_{reversal}$ is significantly skewed to negative values indicating that cargos tend to increase rotation during reversals ($P < 0.0001$ by Kolmogorov-Smirnov test; test statistic, 0.2).

Although acute reversals of WGA axonal endosomes are relatively infrequent, we detected 1470 such reversals in 667 two-channel trajectories

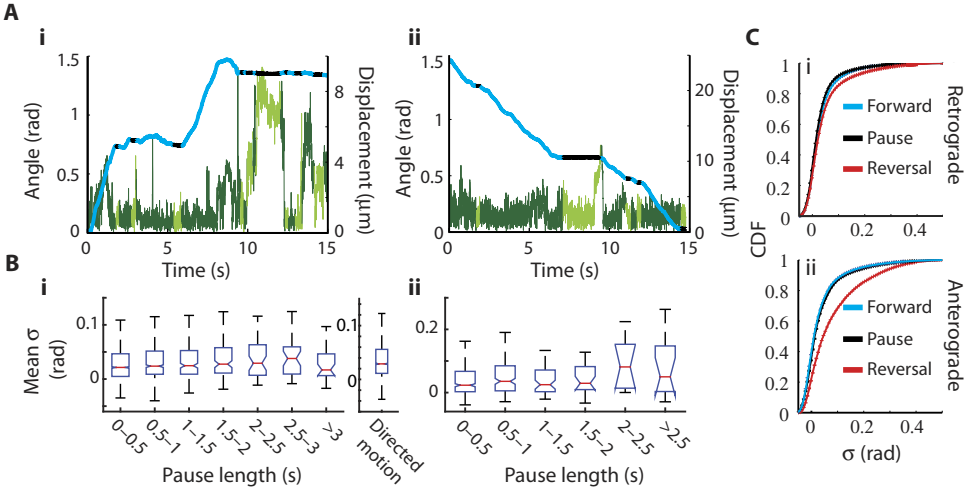

Fig. 6. Endosomes do not increase rotation inside pauses. (**A**) Retrograde-directed (i) and anterograde-directed (ii) endosomes sometimes show translational pauses (directed motion is shown in blue; pauses are shown in black; corresponding orientations are shown in dark and light green, respectively). (**B**) Average rotational lability (σ) does not increase with pause duration for retrograde-directed (i) or anterograde-directed (ii) endosomes. It is also similar to mean σ during directed motion. Red bar is the median value for given pause length, and boxes represent 25th and 75th percentiles with black bars extending to minima and maxima. (**C**) Overall, rotational lability in pauses (black) closely matched directed motion (blue) but was more constrained than during reversals (red) for both net retrograde (top) and net anterograde (bottom) trajectories (±SEM by bootstrapping).

Downloaded from http://advances.sciencemag.org/ on May 27, 2021

(combining retrograde and anterograde). To assess the general rotational dynamics at the point of direction reversal, we analyzed the rotational lability (σ) around the time points where an instantaneous direction reversal occurred (set to zero time in Fig. 7C). We found a significant increase in σ immediately following the reversal at time zero. This trend is not observed in the vicinity of nonreversal velocity changes (red) or randomly selected time points (green) in the same set of trajectories that exhibited reversals. The significance of this difference is confirmed by a two-sample Kolomogrov-Smirnov test comparing the distribution of σ at each time point in all trajectories relative to time zero (fig. S6). These transient increases in rotation can arise from torque exerted on the endosome due to one set of motors binding the microtubule, while the other set is released.

Nanorods align with the underlying microtubule direction

A striking phenomenon we observed in this work was the distinct alignment of the absolute orientation of nanorods inside endosomes with the microtubule tracks on which they traveled. On a long length scale, axonal microtubules run approximately parallel to microchannels, but an axon can tilt slightly and displays local curvatures inside the microchannels. Accordingly, we determined the local orientations of microtubules from the translational trajectory of endosomes (*26*). Because we know the angle of the axon relative to the polarizers used for imaging, we can directly calculate the angle of the nanorod relative to the microtubule on which it travels. The relative angle between the nanorod orientation and the microtubule track is computed for all trajectories and all time points in a trajectory. This is reported as "alignment," ranging from parallel (0 rad) to perpendicular (π/2) to the microtubule. We see a distinct bias toward parallel alignment between an endosomal nanorod and its microtubule track for both anterograde- and retrograde-directed cargos (Fig. 8A). We rule out any bias in the optical setup because alignment results are consistent regardless of how we mount the microchannels relative to the detection optics. Furthermore, these results are consistent for both the two-channel and the three-channel setups and across different batches of DRG cultures (fig. S7). We also computed the median angle between the nanorod and the microtubule track over the course of each nanorod trajectory. The distribution of this angle shows that most of the axonally transported nanorods (~88%) are aligned with the microtubules within π/8 rad (fig. S8).

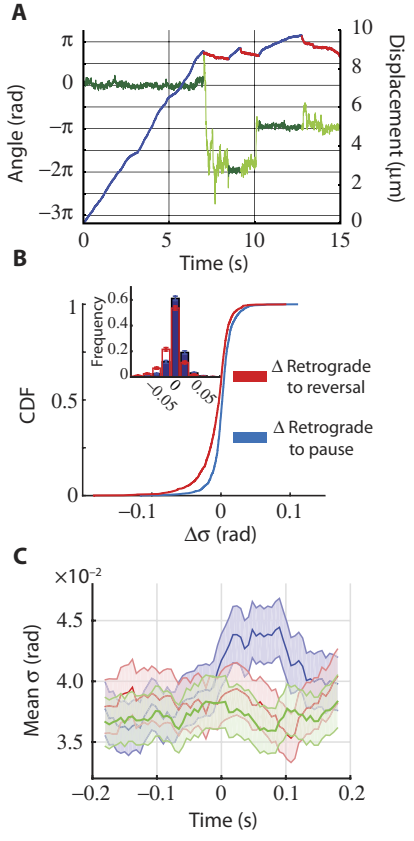

Fig. 7. Endosomes increase rotation following reversals. (**A**) A representative endosome undergoing reversals clearly shows elevated rotation during reversals. Retrograde translocation is colored blue, reversals are colored red, and the corresponding angle points are colored dark greed and light green, respectively. (**B**) Distribution of change in mean σ from retrograde motion to pauses (blue) versus retrograde motion and reversals (red) in net retrograde trajectories. Histogram of the same distribution inset (error bars, 95% confidence interval by bootstrapping). (**C**) Alignment of reversals at zero time shows average σ (blue) increases significantly after reversal more than after nonreversal velocity changes (red) and random points (green) in the same set of trajectories (error bounds ± SEM).

This alignment cannot be explained by a trivial hydrodynamic effect. Figure 8B shows that the alignment angle is not correlated with transport speed in either retrograde (Fig. 8B) or anterograde (fig. S9) directions. Specifically, the nanorod alignment is similar between paused and translocating endosomes. Because hydrodynamic forces experienced by endosomes scale with translational speed, our results rule out the possibility that hydrodynamic forces during transport induce oblong endosomes to align gold nanorods. The rotational lability, which would be predicted to decrease with velocity if the alignment is a hydrodynamic effect, is similarly independent of velocity (Fig. 8B, bottom). Furthermore, even if we assume that the endosome is oblong instead of spherical, for reasonable transport velocities, the Stokes drag for transporting aligned to the microtubule versus perpendicular is similar (see fig. S10 and the Supplementary Materials). Finally, the detection of some endosomes transporting processively at perpendicular orientations is also inconsistent with a purely hydrodynamic explanation (fig. S11).

The nanorod-microtubule alignment appears to be directly related to microtubule binding and microtubule-based transport. Figure 8C (movie S8) shows a trajectory where several pauses exhibit clear translational diffusive motion consistent with unbinding from the microtubule track. The movie and the *x*-*y* plot (Fig. 8C, ii) of the same trajectory clearly show endosomal detachment at the marked pausing periods (red boxes). At these diffusive pausing periods, the endosome displays large fluctuations in orientation consistent with diffusional tumbling depicted in Fig. 1 (condition 1). This is evident in comparing the alignment distribution during the initial pause and the processive motion indicated by the cyan dashed box in Fig. 8C (inset). However, as soon as the endosome rebinds to the microtubule and starts directional transport, the nanorod angle is suddenly fixed at an integer multiple of π radians relative to the angle of the microtubule.

We hypothesize that the nanorod alignment is due to a mechanical linkage between receptors of WGA and microtubule-binding proteins such as molecular motors. Each nanorod is functionalized with an average of 36 WGA dimers and is thus expected to bind to the extracellular domain of many plasma membrane proteins. To test this hypothesis, we attempted to induce nanorod transport with a reduced number of WGA molecules on each nanorod. This was accomplished by initially incubating the nanorods with biotin-BSA to occupy a portion of the available streptavidin sites on the nanorod. Afterward, excess biotin-WGA was added to fill in the remaining sites. Blocking by

Downloaded from http://advances.sciencemag.org/ on May 27, 2021

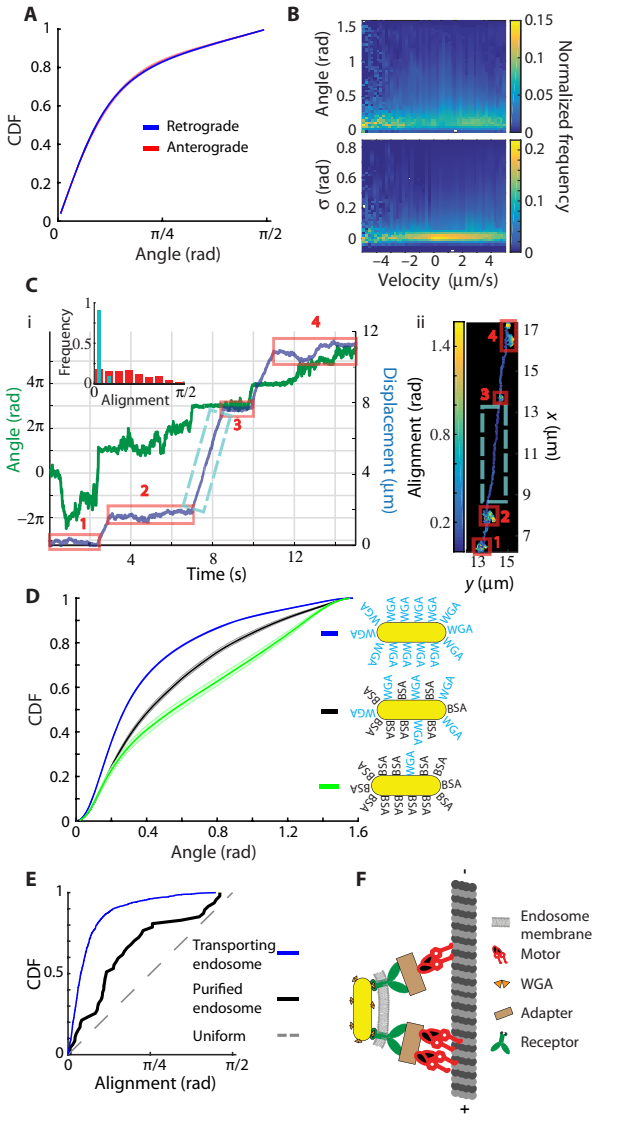

Fig. 8. WGA-nanorod-endosomes align in direction of transport. (**A**) The cumulative distribution of all processive retrograde (1472 trajectories; blue) and anterograde (231 trajectories; red) angles measured in three-channel imaging shows clear preference for alignment (zero angle) with microtubules. Error bars ± SEM from bootstrapping. (**B**) Neither absolute angle of the nanorod (top) nor rotational lability (bottom) is a strong function of velocity in retrograde-directed endosomes. (**C**) Rarely, endosomes show clear detachments from the microtubules (marked with red boxes) accompanied by much less constrained diffusion (movie S8). The alignment is much more uniformly distributed during the first pause as compared to the processive movement indicated by the dashed cyan box (distribution inset). This is evident in an *x*-*y* time projection plot (ii) where each frame in the trajectory is colored by its angle relative to the microtubule. (**D**) Retrograde-directed nanorods fully loaded with WGA show a high degree of alignment in two-channel microscopy (blue; $n = 1736$ endosomes). Reducing the number of WGA by blocking streptavidins with 10 times more biotin–bovine serum albumin (BSA) than nanorods leads to a reduced degree of alignment (black; $n = 211$). Further reducing the number of WGA (blocking with 1:60 nanorod/biotin-BSA) leads to even less alignment (green; $n = 68$). Shaded error bars represent ± SEM from bootstrapping. (**E**) Cumulative distribution of purified nanorod-containing endosomes (solid black line) also shows alignment with microtubules in vitro ($n = 47$ endosomes) compared with a uniform distribution (dashed gray line), although not as much as the median nanorod alignment during transport (blue line; same data as retrograde data from fig. S8). (**F**) Proposed mechanism of alignment featuring a direct linkage between ligand and microtubule through the endosomal membrane.

biotin-BSA was done at low (10:1) and high (60:1) molar ratios to the nanorods.

We found overall transport to be significantly reduced in both cases, consistent with the importance of WGA as the ligand allowing for endocytosis and transport. We used two-channel microscopy to compare the alignment between no biotin-BSA blocking (Fig. 8D, blue), low blocking ratios (Fig. 8D, black), and high blocking ratios (Fig. 8D, green). We find that the alignment is significantly reduced as fewer WGAs are bound to the nanorod. Nanorods under the unblocked condition are at orientations greater than π/4 only 14% of the time. By contrast, under the 10:1 BSA blocking condition, this quantity increases to 25% and increases further to 38% under the 60:1 BSA blocking condition. This increase from low blocking to high blocking is statistically significant ($P = 0.02$ by Kolmogorov-Smirnov test; test statistic, 0.21).

To further test the contribution of the physical linkage (between nanorod and receptor) to the observed alignment of nanorods with microtubules, we attempted to cleave the linkage after endocytosis. We conjugated a photocleavable biotin–*N*-hydroxysuccinimide (NHS) tag instead of regular biotin-NHS onto unlabeled WGA [henceforth referred to as photocleavable biotin (PCB)–WGA]. We then incubated the neurons with PCB-WGA–coated nanorods and allowed them to be endocytosed and transport to be initiated. Next, we illuminated the whole culture with 365-nm light at 40 mW/cm^2 for 30 s to cleave the photocleavable linker of the PCB-WGA linking the nanorod to the receptor in the endosomal lumen. Cultures were then allowed to recover for 5 min before imaging. We measured transport and alignment of 162 endosomes for PCB-WGA nanorods with ultraviolet (UV) treatment and 93 endosomes for PCB-WGA nanorods with no UV treatment. As a control, we performed the same UV illumination with nanorods conjugated to regular biotin-WGA ($n = 189$ endosomes). We found that PCB-WGA–coated nanorods following UV treatment are less aligned to microtubules than biotin-WGA–coated nanorods whose linker remains intact (see the Supplementary Materials and fig. S12).

To test whether alignment to microtubules is due to factors on the endosome, we measured alignment of isolated nanorod-containing endosomes to microtubules in vitro (Fig. 8E and fig. S13). Endosomes containing nanorods were isolated from 4th day in vitro (DIV4) cortical neurons, with the endosomal membrane simultaneously stained with 3,3′-dioctadecyloxacarbocyanine perchlorate (DiO). Isolated endosomes were immediately mixed with freshly polymerized microtubules for 20 min to allow binding before the mixture was adsorbed to the surface of a glass coverslip for imaging. Only nanorods that colocalized with DiO and microtubules were chosen for analysis. The distribution of angles between the nanorod and the microtubule that the endosome is bound to is statistically different from a uniform distribution ($P = 0.0002$ by one-sample Kolmogorov-Smirnov test; test statistic, 0.31). Specifically, ~40% of endosomes had nanorods aligned within π/8 rad of the microtubule, and only ~15% of endosomes had nanorods perpendicular to the microtubule (angle between 3π/8 and π/2). This difference is significant ($P = 0.0035$ by binomial test). Although the proportion of alignment is less than during transport (Fig. 8E, blue curve), alignment even in a purified system is consistent with a mechanical linkage between the ligand-receptor complex in the endosome and the microtubule, as proposed in Fig. 8F.

DISCUSSION

While there has been tremendous work done in vitro to elucidate molecular mechanisms of single cytoskeletal motor motility, reconstituted

Downloaded from http://advances.sciencemag.org/ on May 27, 2021

multimotor transport systems fail to capture all observed transport dynamics in vivo [experimental (*32*) and theoretical (*33*)]. The discrepancy likely arises because of cellular regulation of motor activity through adaptors and geometric arrangements on cargos that support a particular pattern of transport. Many such mechanisms have been hinted at previous studies (*8*, *9*, *34*), but one cannot ascribe any given pause or velocity change inside a cell to a particular mechanism. The ability to make this assignment will demand measuring several degrees of freedom with high precision. Here, we demonstrate that dark-field microscopy with two or three polarization channels maintains high spatiotemporal resolution while also measuring orientation of gold nanorods as an additional degree of freedom. Further, combination with a microfluidic culture platform allows for high data throughput and experimental control, both of which are necessary for study of heterogeneous systems such as axonal transport. For future studies, our method is also fully compatible with simultaneous fluorescence for identifying specific molecular components involved.

Critically, we show that many rotational motions correspond to translational motion phenomena previously shown to result from underlying motor dynamics (for example, changes in cargo velocity). However, rotational and translational dynamics are not always correlated. Often, we observe distinct changes in the rotational state of endosomes despite no significant change in translational motion and vice versa (fig. S3). This is expected because changes in the activity of the motor team can map onto either rotational motion, translational motion, both, or neither. Consequently, rotational motion is an important state variable to measure experimentally to complement information gleaned from translational motion.

By monitoring rotational motion during pauses in transport, we were also able to show that, in DRG axons, endosomes remain highly rotationally constrained during pauses, indicating continued tethering of the endosome to the microtubule even during long pauses. Full detachment may lead to diffusion of the active motors away from the microtubule track leading to slow rebinding, as has been suggested previously (*14*). This delayed rebinding is also evident in this work for the rare endosomes that detach from the microtubules (Fig. 8C). Stable tethering to the microtubules may be important for the robust transport necessary to efficiently move cargos through axons that are orders of magnitude longer than most cell types.

We also show that endosome rotation increases when cargos switch between kinesin- and dynein-driven motion. The magnitude of this increase is significantly larger for kinesin-to-dynein switching compared to dynein-to-kinesin switching. This is to say that endosomes driven primarily by dynein are more rotationally confined during reversals than reversing kinesin-driven endosomes. This rotational confinement is consistent with dynein's higher propensity for backstepping under load (*35*) relative to that of kinesin (*36*). More work needs to be done to determine the cause of the observed difference.

Finally, we observe that, despite being inside an endosome, the nanorods we observe are distinctly aligned with the microtubules in the axon. This alignment cannot be explained by factors such as alignment due to hydrodynamic drag or local axonal environment. We hypothesize that the nanorod alignment with microtubules is caused by a linkage between the WGA-receptor complex and molecular motor complex. The molecular motor complex includes the motor heavy chain as well as associated processivity factors such as dynactin or other microtubule-associated proteins. Previous studies have shown that certain ligand-receptor complexes remain bound inside endosomes and that their physical interaction is important for recruiting transport effectors (*34*, *37*). There is also evidence for direct interactions between receptors and microtubule motors (*38*), but this interaction has not been directly demonstrated in live cells. Cholesterol microdomains, which have been postulated as force generation foci, could also produce similar alignment (*39*). We propose that the presence of many WGA molecules on each nanorod allows for multiple such interactions, which leads to alignment of the nanorod with the microtubule. A tight mechanical linkage also helps explain the relatively restricted overall rotational lability of nanorod-endosomes as well as the readily observable correlations of nanorod orientational dynamics with explicit motor dynamics such as switching between kinesin- and dynein-driven motion.

MATERIALS AND METHODS

Experimental design

Experiments were designed to determine the resolution of the microscopy systems and then use those systems for monitoring endosomal transport in axons. Data were collected to show the relevance of rotation as an observable and relevant feature of axonal transport. Subsequently, rotational data were analyzed during special instances of translational motion previously thought to result from specific changes in motor activity, but there were no specific expectations for how rotational dynamics would correlate with translational dynamics. Nanorod alignment with microtubules was an unexpected observation, although nanorods were expected to be constrained within the endosomes.

Sample sizes for all measurements were selected by collecting data until the resulting distributions (for example, nanorod angle in Fig. 8) converged even when subsets of trajectories or whole experiments were withheld from the analysis. Individual endosome trajectories were tracked if they exhibited some directed motion during the trajectory. Because individual movies were less than a minute, this excluded endosomes that were paused during the entire trajectory because these were difficult to distinguish from free nanorods outside the axons. All trajectories resulted from 25 independent experiments for two-channel data and 15 for three-channel data.

Cell culture

DRG neurons were dissected out of embryonic day 18 (E18) Sprague-Dawley rat embryos and grown in culture for 6 to 14 days, as described previously (*40*). Briefly, DRGs were dissected out of embryos in Hanks' buffered saline solution and treated with 0.25% trypsin for 30 min followed by mechanical trituration. Trypsin was quenched by the addition of equal volume of Dulbecco's modified Eagle's medium + 10% fetal bovine serum, and dissociated cells were spun down. Cells were subsequently resuspended in 1 ml of maintenance media [neurobasal, B27, 2 mM L-glutamine/GlutaMAX, penicillin-streptomycin (100 U/ml), and nerve growth factor (50 ng/ml)]. After counting the cell density, cells were spun down and resuspended in maintenance media to a final concentration of 25 million cells/ml. Four microliters of suspended cells was plated in the cell body compartment of the microfluidic chamber. Cells were maintained at 37°C and 5% CO_2 for 6 to 12 days. On day 1, the maintenance medium was supplemented with 1 μM cytosine arabinoside for 1 day to restrict glial cell proliferation. Rats used in this study were treated in accordance with Stanford University's institutional guidelines.

Gold nanorod conjugation

Streptavidin-functionalized gold nanorods were purchased from Nanopartz (part number C12-25-650-TS-PBS-50). Nanorod dimensions are 25 nm in diameter and 71 nm in length. Biotin-WGA was purchased from Vector Laboratories (B-1025).We prepared WGA-functionalized gold

Downloaded from http://advances.sciencemag.org/ on May 27, 2021

nanorods by incubating ~1.5×10^{10} streptavidin-conjugated nanorods with biotin-WGA (1:200 molar ratio, nanorod/biotin-WGA) for 20 min in a volume of <10 μl. Subsequently, the gold nanorod suspension was diluted 20-fold with PBS and centrifuged at 8000*g* for 5 min at room temperature to remove unconjugated WGA. After washing, WGA-nanorods were resuspended in a final volume of 25 μl (final concentration, ~1 nM nanorods) of maintenance medium. The freshly prepared nanorod suspension was immediately added to either the axon compartment or the cell body compartment and incubated at 37°C for 1.5 hours in 5% CO_2. Imaging was performed in CO_2-independent media.

For the experiment in Fig. 8D, the conjugation was largely the same, but nanorods were first incubated with biotin-BSA at a molar ratio of 1:10 or 1:60 for 5 min. Biotin-WGA was then added at a 1:200 nanorod/biotin-WGA ratio for 20 min.

Imaging

For imaging, culture chambers were sandwiched with an additional coverslip on top of the microfluidic chamber. Imaging was done on an inverted Nikon microscope (Eclipse Ti-U) using an adjustable NA 60× oil immersion objective set to ~1.1 NA and a 1.4-NA oil immersion condenser. The objective and the microscope stage were heated so the imaging area was held at 31°C for transport assays and at room temperature for surface-bound nanorods in Fig. 3. Samples were imaged for no more than 30 min to avoid artifacts from deteriorating the health of cells.

For the imaging optics, we used a modified 4f imaging setup. One 200-mm focal length lens was positioned one focal length from the image plane of the microscope tube lens. After this, the image was split either by a polarizing beamsplitting cube (two-channel) or by a nonpolarizing beamsplitting cube (three-channel). The second 200-mm focal length was positioned in the optical path, as shown in Fig. 2A.

All samples were imaged with 2-ms exposure per frame for two-channel imaging and 4-ms exposure per frame for three-channel imaging. Acquisition was done at 166 Hz unless otherwise specified. Images were captured using a pco.edge sCMOS camera operating in rolling shutter mode.

Nanorod rotational lability assays (Fig. 4)

For glass surface–bound nanorods, nanorods were diluted 1000-fold in PBS containing 1 mM calcium chloride and immediately added to glass coverslips and allowed to nonspecifically adhere. For lipid bilayers, coverslips were initially cleaned with piranha and plasma cleaning, followed by formation of bilayer from L-α-phosphatidylcholine lipids doped with 1 mole percent (mol %) 1,2-dioleoyl-*sn*-glycero-3-phosphoethanolamine-*N*-(cap biotinyl) and 0.5 mol % Texas Red–1,2-dihexanoyl-*sn*-glycero-3-phosphoethanolamine (Avanti Polar Lipids) to which nanorods were added. For cell surface binding, nanorods were conjugated to biotin-WGA, as described above, and added to COS-7 cells pretreated with 100 nM Latrunculin B to prevent endocytosis. Imaging was done after 5-min incubation and extensive washing.

Microtubule preparation

Microtubules for experiments in Fig. 8E were prepared by making a solution of unlabeled tubulin (0.8 mg/ml), biotinylated tubulin (0.15 mg/ml), and tetramethylrhodamine-labeled tubulin (0.15 mg/ml) in BRB80 [80 mM Pipes, 1 mM $MgCl_2$, and 1 mM EGTA (pH 6.8)] with 10% dimethyl sulfoxide and 1 mM guanosine triphosphate. The mixture was incubated at 37°C for 20 min. Taxol (20 μM) and 1 mM dithiothreitol (DTT) were added, and then the mixture was incubated for another 20 min.

Endosome purification

Endosomes for data in Fig. 4 were purified, as previously described (*41*). Briefly, DRG neurons were grown in mass culture to DIV7 and incubated with nanorod-biotin-WGA as for transport experiments in maintenance media supplemented with 10 μM FM1-43 to label plasma membrane–derived cargo. Cells were washed several times after nanorod incubation with PBS, then removed mechanically from the surface, and homogenized in a Dounce homogenizer. Most free nanorods were removed by the wash step, but further confirmation of endosomes was done by measuring colocalization with FM1-43 signal.

For endosome-microtubule alignment experiments in Fig. 8E, E18 rat cortical neurons were plated at high density on poly-L-lysine–coated coverslips. Cells were grown to DIV4 and incubated with 0.1 nM WGA-nanorod particles for 20 min in PBS with 4 μM DiO to label membranes. The nanorod solution was replaced with maintenance media without nanorods for an additional 10 min. Cells were then washed with ice-cold PBS, and postnuclear supernatant (PNS) was prepared as in the study of Gorvel *et al.* (*42*). PNS was incubated with tetramethylrhodamine-labeled microtubules for 20 min in homogenization buffer [25 mM Mops (pH 7.0), 75 mM KCl, casein (1 mg/ml), 250 mM sucrose, 3 mM imidazole, 1 mM EGTA, 1 mM $MgCl_2$, 1 mM DTT, and 20 μM taxol] at room temperature and then allowed to attach nonspecifically to glass coverslips for 5 min. Free complexes were washed out, and only nanorods that also showed DiO signal and colocalization with microtubules were used for analysis (see example images in fig. S12). Data in Fig. 8E are from 47 nanorod-endosomes from three independent endosome preparations.

PDMS microchannel culture device fabrication

PDMS microchannel culture devices were prepared, as described by Zhang *et al.* (*26*). Briefly, master patterns were made on silicon wafers using photolithography. PDMS was then prepared by mixing degassed silicone elastomer and curing agent (10:1, w/w ratio) and poured over the silicon wafer, followed by curing at 70°C overnight. Axon and cell body chambers were then manually cut out on each side of the microchannels.

Single-particle tracking and angle calculation

Processive nanorod-endosomes were identified as bright motile point spread functions in the transport movies. A custom MATLAB routine was used to identify nanorod trajectories and perform two-dimensional Gaussian fits in each polarization channel for each frame of the movie (section S1). For two-channel angle calculation, the angle was quadrant degenerate, and was calculated as

$$\varphi = \tan^{-1}\sqrt{\frac{I_p}{I_0}} \quad (1)$$

where I_0 is the reference polarization channel (0) and I_p is the second polarization channel (π/2). Total scattering intensity detected is affected by many factors, but φ can be determined without knowing the total scattered intensity by using any two polarization channels where the first channel is defined as 0 and the second channel is offset by some angle α

$$\varphi = \tan^{-1}\left[\frac{\cos(\alpha)\pm\sqrt{\frac{I_p}{I_0}}}{\sin(\alpha)}\right] \quad (2)$$

In the two-channel case, α is just π/2, and Eq. 2 becomes Eq. 1. For the three-channel angle calculation, φ was thus calculated for each

Downloaded from http://advances.sciencemag.org/ on May 27, 2021

combination of two channels. The accepted solution came from the combination of channels that had the highest combined rate of intensity change as a function of azimuthal angle ($|dI_p/d\varphi - dI_0/d\varphi|$). Using the 0 and π/2 channels leaves the aforementioned degeneracy. Thus, if the highest rate of intensity change came from the 0 and π/2 channels, the sign of the angle was taken from the next highest intensity change channel pair (resolving the degeneracy). For full angle resolution, adjacent frames were shifted by −π, 0, or π rad to minimize frame-to-frame angle differences.

Translational motion was further decomposed into motion parallel and perpendicular to the microtubule track, as in the study of Chowdary *et al.* (*11*). All translational motion analyses were done using motion parallel to the microtubule track, unless otherwise specified.

Pause and reversal determination

Pauses were automatically identified on the basis of mean square displacement analysis and asymmetry of motion in a 0.5-s sliding window, as in the study of Chowdary *et al.* (*11*). Briefly, the trajectory was characterized by several parameters in the window ($w = 83$ frames). These include the mean square displacement (*msd*) and asymmetry in motion (*Asym*) given by the eigenvalues of the radius of gyration tensor, R_1 and R_2

$$\left\langle \mathrm{msd}(\tau = n\Delta t)\right\rangle = \frac{1}{N_w - n}\sum_{j=x,y}\sum_{k=1}^{N_w-n}\left[q_j((k+n)\Delta t) - q_j(k\Delta t)\right]^2 \quad (3)$$

$$\mathrm{Asym} = -\log\left[1 - \frac{(R_1 - R_2)^2}{(R_1 + R_2)^2}\right] \quad (4)$$

Fitting the mean square displacement curve to Eq. 3 gives α

$$\left\langle \mathrm{msd}(\tau)\right\rangle = 4D\tau^{\alpha} + 2(\sigma^I)^2 \quad (5)$$

where σ^I is the localization uncertainty of the imaging system and $q(t)$ is the position of the endosome at time t. Pauses were defined as segments of the trajectory where $\mathrm{Asym}(t) < 1.75$ and $\alpha(t) < 1.4$.

Points of reversal were determined through automatic trajectory parsing (*11*), followed by manual selection of automatically detected reversals to remove false positives resulting from instrument noise or vibration artifacts.

Adjusted σ calculation

σ was calculated as the SD of the calculated angle within a sliding window of 11 frames (66 ms). This window size was chosen to be sufficiently sensitive to detect single fast rotations but small enough of the angle data to account for sampling error. The angle calculation is subject to noise that is a function of both azimuthal angle and total detected intensity. To control for this statistical noise, σ was calculated for >200 gold nanorods immobilized on glass with varying intensities (fig. S1), and a reference set of a baseline σ as a function of intensity and calculated angle was computed. The corresponding reference σ was subtracted from transporting endosomes. This can sometimes result in negative values of σ.

Statistical analysis

Cross-correlation analysis for translational motion/rotational motion correlation

Linear acceleration and rotational velocity were computed by linear fitting in an 11-frame (66 ms) window for each individual trace. Global mean acceleration and rotational velocity, $\langle d^2r/dt^2\rangle$ and $\langle da/dt\rangle$, respectively, were computed using all transport traces. Cross-correlations were computed for individual traces according to the equation below

$$X(m) = \frac{\sum_{i=s}^{f}\left\{\left[\frac{d}{dt}a(i+m) - \left\langle\frac{da}{dt}\right\rangle\right]*\left[\frac{d^2}{dt}r(i) - \left\langle\frac{d^2r}{dt^2}\right\rangle\right]\right\}}{\sqrt{\sum_{i=s}^{f}\left[\frac{d}{dt}a(i+m) - \left\langle\frac{da}{dt}\right\rangle\right]^2}*\sqrt{\sum_{i=s}^{f}\left[\frac{d^2}{dt^2}r(i) - \left\langle\frac{d^2}{dt^2}\right\rangle\right]^2}} \quad (6)$$

where a is the angle, m is the lag of the cross-correlation, r is the displacement of the endosome, t is the time, s is the first frame used for the cross-correlation, and f is the final frame. Trace cross-correlations were averaged over all traces for retrograde or anterograde conditions. Cross-correlations between angle and acceleration were compared to a control analysis that performed the same calculation but taking the original angle signal and switching the first and second halves of the time course. This maintains the exact patterns and magnitudes of angle changes in the real data but decouples the time for the angle and displacement data.

Statistical distribution generation

Distributions in the following figures are generated by pooling relevant measurement values at each frame of each movie (that is, one movie produces 2500 frames, so 2500 data points; Figs. 4C, 6C, and 8, A, B, and D, and fig. S9). Because adjacent frames within a trajectory are not independent, but individual trajectories are, bootstrapping for these figures was done by resampling individual trajectories and using all their data points instead of resampling individual frames. For the same reason, significance determination by Kolmogorov-Smirnov test for differences in distributions was done assuming a sample size equal to the number of trajectories instead of the number of frames. Individual data points for Figs. 4E, 5 (B and D), and 6C result from appropriate summary statistic for a given segment (mean and median) of trajectory. Data for Fig. 7B and fig. S8 represent summary statistics for whole individual trajectories, and thus these points are independent. We set the threshold for significance unless otherwise specified as $P < 0.05$ as is common practice.

SUPPLEMENTARY MATERIALS

Supplementary material for this article is available at http://advances.sciencemag.org/cgi/content/full/4/3/e1602170/DC1

section S1. Endosome position determination
section S2. Rotation of detached endosome
section S3. Estimation of endosome size and hydrodynamic drag during transport
section S4. Reduction in nanorod-microtubule alignment after disruption of the ligand-receptor interaction
fig. S1. System precision calibration.
fig. S2. Estimation of minimal imaging speed from freely tumbling endosome.
fig. S3. Different pauses of the same endosome can be rotationally distinct.
fig. S4. Angular velocity correlates with motion of the endosome perpendicular to the microtubule.
fig. S5. Endosome rotational motion is not a function of local axonal environment.
fig. S6. Reversals have statistically significant increase in rotation.
fig. S7. Alignment distribution in individual experiments.
fig. S8. Median endosome orientation is still aligned with microtubules.

Downloaded from http://advances.sciencemag.org/ on May 27, 2021

fig. S9. Anterograde endosome alignment not due to hydrodynamic forces.
fig. S10. Rotational tracking of freely diffusing endosome in the axon.
fig. S11. Orientational memory maintained for orientations perpendicular to the microtubule track.
fig. S12. Alignment of nanorods to microtubules after ligand-receptor interaction cleavage.
fig. S13. Sample nanorod-endosome-microtubule images.
movie S1. Corresponds to fig. S2.
movie S2. Corresponds to trace in Fig. 3D in the main text.
movie S3. Corresponds to bottom kymograph in Fig. 3C the main text.
movie S4. Retrograde-directed endosome from Fig. 5A showing correlations between angular velocity and translational acceleration.
movie S5. Corresponds to Fig. 6A in the main text.
movie S6. Corresponds to Fig. 7C in the main text.
movie S7. Corresponds to Fig. 7A in the main text.
movie S8. Corresponds to Fig. 8C in the main text.
Reference (*43*)

REFERENCES AND NOTES

1. X. Wang, D. Winter, G. Ashrafi, J. Schlehe, Y. L. Wong, D. Selkoe, S. Rice, J. Steen, M. J. LaVoie, T. L. Schwarz, PINK1 and Parkin target Miro for phosphorylation and degradation to arrest mitochondrial motility. *Cell* **147**, 893–906 (2011).
2. L.-S. Her, L. S. B. Goldstein, Enhanced sensitivity of striatal neurons to axonal transport defects induced by mutant huntingtin. *J. Neurosci.* **28**, 13662–13672 (2008).
3. K. Zhang, R. Fishel Ben Kenan, Y. Osakada, W. Xu, R. S. Sinit, L. Chen, X. Zhao, J.-Y. Chen, B. Cui, C. Wu, Defective axonal transport of Rab7 GTPase results in dysregulated trophic signaling. *J. Neurosci.* **33**, 7451–7462 (2013).
4. S. P. Gross, M. Vershinin, G. T. Shubeita, Cargo transport: Two motors are sometimes better than one. *Curr. Biol.* **17**, R478–R486 (2007).
5. V. Soppina, A. K. Rai, A. J. Ramaiya, P. Barak, R. Mallik, Tug-of-war between dissimilar teams of microtubule motors regulates transport and fission of endosomes. *Proc. Natl. Acad. Sci. U.S.A.* **106**, 19381–19386 (2009).
6. A. G. Hendricks, E. Perlson, J. L. Ross, H. W. Schroeder III, M. Tokito, E. L. F. Holzbaur, Motor coordination via a tug-of-war mechanism drives bidirectional vesicle transport. *Curr. Biol.* **20**, 697–702 (2010).
7. S. E. Encalada, L. Szpankowski, C.-h. Xia, L. S. B. Goldstein, Stable kinesin and dynein assemblies drive the axonal transport of mammalian prion protein vesicles. *Cell* **144**, 551–565 (2011).
8. M.-m. Fu, E. L. F. Holzbaur, JIP1 regulates the directionality of APP axonal transport by coordinating kinesin and dynein motors. *J. Cell Biol.* **202**, 495–508 (2013).
9. E. Klinman, E. L. F. Holzbaur, Stress-induced CDK5 activation disrupts axonal transport via Lis1/Ndel1/dynein. *Cell Rep.* **12**, 462–473 (2015).
10. J. P. Pandey, D. S. Smith, A Cdk5-dependent switch regulates Lis1/Ndel1/dynein-driven organelle transport in adult axons. *J. Neurosci.* **31**, 17207–17219 (2011).
11. P. D. Chowdary, D. L. Che, K. Zhang, B. Cui, Retrograde NGF axonal transport—Motor coordination in the unidirectional motility regime. *Biophys. J.* **108**, 2691–2703 (2015).
12. M. J. I. Müller, S. Klumpp, R. Lipowsky, Bidirectional transport by molecular motors: Enhanced processivity and response to external forces. *Biophys. J.* **98**, 2610–2618 (2010).
13. J. Y. Yi, K. M. Ori-McKenney, R. J. McKenney, M. Vershinin, S. P. Gross, R. B. Vallee, High-resolution imaging reveals indirect coordination of opposite motors and a role for LIS1 in high-load axonal transport. *J. Cell Biol.* **195**, 193–201 (2011).
14. R. P. Erickson, Z. Jia, S. P. Gross, C. C. Yu, How molecular motors are arranged on a cargo is important for vesicular transport. *PLOS Comput. Biol.* **7**, e1002032 (2011).
15. A. Kunwar, A. Mogilner, Robust transport by multiple motors with nonlinear force-velocity relations and stochastic load sharing. *Phys. Biol.* **7**, 16012 (2010).
16. G. Arpağ, S. Shastry, W. O. Hancock, E. Tüzel, Transport by populations of fast and slow kinesins uncovers novel family-dependent motor characteristics important for in vivo function. *Biophys. J.* **107**, 1896–1904 (2014).
17. F. Berger, C. Keller, S. Klumpp, R. Lipowsky, External forces influence the elastic coupling effects during cargo transport by molecular motors. *Phys. Rev. E Stat. Nonlin. Soft Matter Phys.* **91**, 022701 (2015).
18. F. Berger, C. Keller, R. Lipowsky, S. Klumpp, Elastic coupling effects in cooperative transport by a pair of molecular motors. *Cell. Mol. Bioeng.* **6**, 48–64 (2013).
19. A. R. Driller-Colangelo, K. W. L. Chau, J. M. Morgan, N. D. Derr, Cargo rigidity affects the sensitivity of dynein ensembles to individual motor pausing. *Cytoskeleton* **73**, 693–702 (2016).
20. S. Ayloo, J. E. Lazarus, A. Dodda, M. Tokito, E. M. Ostap, E. L. F. Holzbaur, Dynactin functions as both a dynamic tether and brake during dynein-driven motility. *Nat. Commun.* **5**, 4807 (2014).
21. T. L. Culver-Hanlon, S. A. Lex, A. D. Stephens, N. J. Quintyne, S. J. King, A microtubule-binding domain in dynactin increases dynein processivity by skating along microtubules. *Nat. Cell Biol.* **8**, 264–270 (2006).
22. Y. Gu, W. Sun, G. Wang, K. Jeftinija, S. Jeftinija, N. Fang, Rotational dynamics of cargos at pauses during axonal transport. *Nat. Commun.* **3**, 1030 (2012).
23. R. H. Lee, C. S. Mitchell, Axonal transport cargo motor count versus average transport velocity: Is fast versus slow transport really single versus multiple motor transport? *J. Theor. Biol.* **370**, 39–44 (2015).
24. C. Sönnichsen, A. P. Alivisatos, Gold nanorods as novel nonbleaching plasmon-based orientation sensors for polarized single-particle microscopy. *Nano Lett.* **5**, 301–304 (2005).
25. J. T. Fourkas, Rapid determination of the three-dimensional orientation of single molecules. *Opt. Lett.* **26**, 211–213 (2001).
26. K. Zhang, Y. Osakada, M. Vrljic, L. Chen, H. V. Mudrakola, B. Cui, Single-molecule imaging of NGF axonal transport in microfluidic devices. *Lab Chip* **10**, 2566–2573 (2010).
27. S. Maday, K. E. Wallace, E. L. F. Holzbaur, Autophagosomes initiate distally and mature during transport toward the cell soma in primary neurons. *J. Cell Biol.* **196**, 407–417 (2012).
28. M. Kempf, A. Clement, A. Faissner, G. Lee, R. Brandt, Tau binds to the distal axon early in development of polarity in a microtubule- and microfilament-dependent manner. *J. Neurosci.* **16**, 5583–5592 (1996).
29. M. R. Galiano, S. Jha, T. S.-Y. Ho, C. Zhang, Y. Ogawa, K.-J. Chang, M. C. Stankewich, P. J. Mohler, M. N. Rasband, A distal axonal cytoskeleton forms an intra-axonal boundary that controls axon initial segment assembly. *Cell* **149**, 1125–1139 (2012).
30. A. K. Rai, A. Rai, A. J. Ramaiya, R. Jha, R. Mallik, Molecular adaptations allow dynein to generate large collective forces inside cells. *Cell* **152**, 172–182 (2013).
31. X. Wang, T. L. Schwarz, The mechanism of Ca^{2+}-dependent regulation of kinesin-mediated mitochondrial motility. *Cell* **136**, 163–174 (2009).
32. N. D. Derr, B. S. Goodman, R. Jungmann, A. E. Leschziner, W. M. Shih, S. L. Reck-Peterson, Tug-of-war in motor protein ensembles revealed with a programmable DNA origami scaffold. *Science* **338**, 662–665 (2012).
33. A. Kunwar, S. K. Tripathy, J. Xu, M. K. Mattson, P. Anand, R. Sigua, M. Vershinin, R. J. McKenney, C. C. Yu, A. Mogilner, S. P. Gross, Mechanical stochastic tug-of-war models cannot explain bidirectional lipid-droplet transport. *Proc. Natl. Acad. Sci. U.S.A.* **108**, 18960–18965 (2011).
34. S.-H. Huang, S. Duan, T. Sun, J. Wang, L. Zhao, Z. Geng, J. Yan, H.-J. Sun, Z.-Y. Chen, JIP3 mediates TrkB axonal anterograde transport and enhances BDNF signaling by directly bridging TrkB with kinesin-1. *J. Neurosci.* **31**, 10602–10614 (2011).
35. A. Gennerich, A. P. Carter, S. L. Reck-Peterson, R. D. Vale, Force-induced bidirectional stepping of cytoplasmic dynein. *Cell* **131**, 952–965 (2007).
36. C. M. Coppin, D. W. Pierce, L. Hsu, R. D. Vale, The load dependence of kinesin's mechanical cycle. *Proc. Natl. Acad. Sci. U.S.A.* **94**, 8539–8544 (1997).
37. A. W. Harrington, C. St. Hillaire, L. S. Zweifel, N. O. Glebova, P. Philippidou, S. Halegoua, D. D. Ginty, Recruitment of actin modifiers to TrkA endosomes governs retrograde NGF signaling and survival. *Cell* **146**, 421–434 (2011).
38. H. Yano, F. S. Lee, H. Kong, J.-Z. Chuang, J. C. Arevalo, P. Perez, C.-H. Sung, M. V. Chao, Association of Trk neurotrophin receptors with components of the cytoplasmic dynein motor. *J. Neurosci.* **21**, RC125 (2001).
39. A. Rai, D. Pathak, S. Thakur, S. Singh, A. K. Dubey, R. Mallik, Dynein clusters into lipid microdomains on phagosomes to drive rapid transport toward lysosomes. *Cell* **164**, 722–734 (2016).
40. J. R. Chan, P. M. Rodriguez-Waitkus, B. K. Ng, P. Liang, M. Glaser, Progesterone synthesized by Schwann cells during myelin formation regulates neuronal gene expression. *Mol. Biol. Cell* **11**, 2283–2295 (2000).
41. A. E. Sgro, S. M. Bajjalieh, D. T. Chiu, Single-axonal organelle analysis method reveals new protein-motor associations. *ACS Chem. Neurosci.* **4**, 277–284 (2013).
42. J.-P. Gorvel, P. Chavrier, M. Zerial, J. Gruenberg, Rab5 controls early endosome fusion in vitro. *Cell* **64**, 915–925 (1991).
43. E. O. Puchkov, Intracellular viscosity: Methods of measurement and role in metabolism. *Biochemistry* **7**, 270–279 (2013).

Acknowledgments

Funding: This work was supported by NIH (grant no. NS057906), a Searle Scholar award, and a Packard Science and Engineering Fellowship (to B.C.). **Author contributions:** L.K. performed all experiments and analysis. L.K. and B.C. designed experiments and wrote the manuscript. A.I. and L.K. performed the purified nanorod-endosome-microtubule binding experiments. P.C. assisted in design of the automatic pause detection algorithm. Z.B. helped design experiments and analyze data for nanorod-endosome-microtubule binding experiments. **Competing interests:** The authors declare that they have no competing interests. **Data and materials availability:** All data needed to evaluate the conclusions in the paper are present in the paper and/or the Supplementary Materials. Additional data related to this paper may be requested from the authors.

Submitted 9 September 2016
Accepted 30 January 2018
Published 7 March 2018
10.1126/sciadv.1602170

Citation: L. Kaplan, A. Ierokomos, P. Chowdary, Z. Bryant, B. Cui, Rotation of endosomes demonstrates coordination of molecular motors during axonal transport. *Sci. Adv.* **4**, e1602170 (2018).

Downloaded from http://advances.sciencemag.org/ on May 27, 2021

Science Advances

Rotation of endosomes demonstrates coordination of molecular motors during axonal transport

Luke Kaplan, Athena Ierokomos, Praveen Chowdary, Zev Bryant and Bianxiao Cui

Sci Adv **4** (3), e1602170.
DOI: 10.1126/sciadv.1602170

ARTICLE TOOLS http://advances.sciencemag.org/content/4/3/e1602170

SUPPLEMENTARY MATERIALS http://advances.sciencemag.org/content/suppl/2018/03/05/4.3.e1602170.DC1

REFERENCES This article cites 43 articles, 14 of which you can access for free
http://advances.sciencemag.org/content/4/3/e1602170#BIBL

PERMISSIONS http://www.sciencemag.org/help/reprints-and-permissions

Use of this article is subject to the Terms of Service

Science Advances (ISSN 2375-2548) is published by the American Association for the Advancement of Science, 1200 New York Avenue NW, Washington, DC 20005. The title *Science Advances* is a registered trademark of AAAS.

Copyright © 2018 The Authors, some rights reserved; exclusive licensee American Association for the Advancement of Science. No claim to original U.S. Government Works. Distributed under a Creative Commons Attribution NonCommercial License 4.0 (CC BY-NC).

Downloaded from http://advances.sciencemag.org/ on May 27, 2021